ACS OMEGA

Open Access

http://pubs.acs.org/journal/acsodf

Article

Anion Effects on the Structural and Magnetic Properties of a Series of Trinuclear Cu^{II}–Ln^{III}–Cu^{II} Complexes

Brodie E. Matheson, Tyson N. Dais, Marryllyn E. Donaldson, Shin-ichiro Takeshi, Liangcheng Lyu, Rina Takano, Takayuki Ishida, Gareth J. Rowlands, and Paul G. Plieger*

Cite This: *ACS Omega* 2025, 10, 50839–50849

Read Online

ACCESS | Metrics & More | Article Recommendations | Supporting Information

ABSTRACT: Two series of heterometallic $Cu^{II}_2Ln^{III}$ complexes, ($[Cu_2Ln(\mathbf{H_4L})_2(MeOH)_2Br](MeOH)_4(Et_2O)(Br_2)$, where Ln = Y (**1**), Gd (**2**), Er (**3**), Tb (**4**)), and ($[Cu_2Ln(\mathbf{H_4L})_2(MeOH)_2Cl_2](MeOH)_4(Et_2O)Cl$, where Ln = Y (**5**), Gd (**6**), Er (**7**), Tb (**8**), and H_6L = (*N*,*N*′-bis(2,3,4-trihydroxybenzylidene)-1,2-phenylenediamine), were designed, synthesized, and characterized through X-ray and magnetic analyses. X-ray analysis revealed that the bromide containing complexes **1**–**4** possessed identical supramolecular arrangements, crystallizing in layers of 2D sheets, while chloride containing complexes **5**–**8** formed a 3D supramolecular lattice possessing an additional π–π stacking interaction per complex. DC magnetic susceptibility measurements showed that complexes **3** and **7** exhibited antiferromagnetic coupling between copper and erbium centers while the gadolinium (**2** and **6**) and terbium (**4** and **8**) containing complexes displayed ferromagnetic Cu—Ln coupling upon cooling. AC magnetic susceptibility measurements revealed that complexes **4** and **8** also displayed zero-field SMM behavior with U_{eff} = 17.8 and 16.0 K, respectively. The larger bromide anion in complex **4** aids in the isolation of the magnetic centers, resulting in a U_{eff} value higher than that of the chloride analogue.

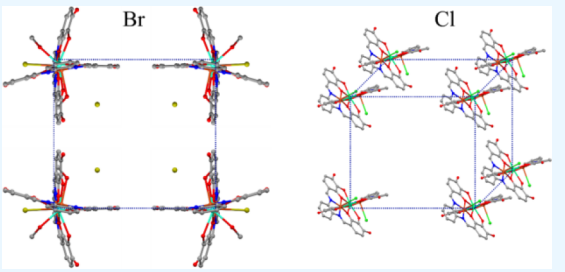

INTRODUCTION

Single-molecule magnets (SMMs) are a class of discrete metal–organic complexes that can be magnetized under an applied magnetic field and subsequently exhibit slow magnetization relaxation below a certain blocking temperature (T_b). One of the more promising avenues of research into SMMs is heterometallic 3d/4f complexes, with the first being the tetranuclear $Cu^{II}_2Tb^{III}_2$ complex reported by Osa et al. in 2004.[1] These complexes combine the high ground-state anisotropy of lanthanide ions with the exchange pathways present in transition metal ions.[2] The potential benefits of this are twofold; first, these exchange pathways provide a route for magnetic coupling between adjacent metal centers that can reduce the probability of quantum tunnelling of the magnetization (QTM), a major contributing factor to the relaxation of magnetization within SMMs.[3] Second, magnetic coupling of lanthanides with paramagnetic transition metal ions can directly improve SMM performance, as shown by Langley and co-workers, who observed that Cr^{III} analogues of Co^{III} 3d/4f complexes exhibited superior SMM behavior.[4,5] However, interactions within 3d/4f systems can also negatively impact the SMM performance. Weak exchange interactions in a series of M_2Ln_2 butterfly complexes (M = Mg^{II}, Mn^{III}, Co^{II}, Ni^{II}, and Cu^{II}; Ln = Y^{III}, Gd^{III}, Tb^{III}, Dy^{III}, Ho^{III}, and Er^{III}) were shown to decrease the effective energy barrier for reversal of magnetization (U_{eff}) by Moreno Pineda et al.[6] Secondary interactions, such as steric hindrance, π–π stacking, and hydrogen bonding, are also of vital importance when designing SMMs.[7−10] Some key factors in the performance of SMMs such as the magnetic isolation of the complexes and the orientation of the magnetic axis are dominated by secondary interactions.[9,11−13] This has been well documented by Tang et al., who utilized bulky macrocyclic ligands to elucidate the relaxation mechanisms of SMMs.[14−17] These ligands effectively isolated the magnetic centers and, combined with in-plane electron withdrawing substituents, which result in electron-poor donors at the metal centers, resulted in a marked increase in U_{eff}.[18]

An effective strategy for elucidating the effects of secondary interactions is through anion substitution.[19−23] A report by Douib et al. demonstrated that the partial substitution of the smaller hfc anion (hfc^- = 3-(heptafluoropropylhydroxymethylene)-(±)-camphorate) with the bulkier BArF anion ($BArF^-$ = tetrakis(3,5-bis(trifluoromethyl)phenyl)borate) resulted in a modification of the supramolecular architecture of the resultant complexes and enhanced the SMM performance of the BArF-substituted complex.[12,23] In this Letter, we

Received: February 8, 2025
Revised: October 9, 2025
Accepted: October 17, 2025
Published: October 23, 2025

describe our investigation into the effect that chloride and bromide anions had on the structural and magnetic properties of a family of heterometallic trinuclear Cu_2Ln (Ln = Y, Gd, Er, Tb, Dy, and Ho) complexes. We synthesized a symmetric trihydroxybenzaldehyde-based Schiff-base ligand capable of forming a trinuclear complex of the form L_2Cu_2LnX, where X = Br or Cl. We expected the chloride containing complexes to have strong directional hydrogen bonding interactions owing to the higher electronegativity of the chloride anion. These stronger interactions were anticipated to decrease the Ln−O−Cu bond angle, promoting ferromagnetic exchange, while the bulkier bromide anion was expected to magnetically isolate the complexes due to steric hindrance. Through X-ray structural analysis, we aimed to determine which of these interactions was dominant. Magnetic analysis then determined which of these interactions was beneficial in enhancing the SMM properties of the resultant complexes. This enabled us to determine which interactions to focus on when developing new SMMs.

EXPERIMENTAL SECTION

All starting materials and solvents were obtained from commercial sources and used without purification, unless otherwise stated. MeOH was dried according to the procedure of Lund and Bjerrum and then stored over activated 3 Å molecular sieves for a week prior to use.[24]

Instrumentation. All NMR spectra were collected at RT on a Bruker 500 Avance instrument; all shifts are reported relative to the residual solvent signal. ESI-MS spectra were collected on a Dionex UltiMate 3000. ATR-IR spectra were collected on a Nicolet 5700 IR instrument using a diamond ATR sampling accessory. Melting point measurements were collected on a Gallenkamp melting point apparatus and are uncorrected. CHN elemental analyses were collected by the Elemental Microanalysis Service, Department of Molecular Sciences, Macquarie University.

X-ray Crystallography. Single-crystal X-ray data were collected on a Bruker D8 Venture instrument equipped with a IμS 3.0 Microfocus Cu−Kα source (λ = 1.54178 Å) and a PHOTON III detector. Crystals were mounted on MiTeGen mylar loops using Fomblin Y oil and cooled to 100 K using an Oxford Cryostream 800. The data was collected and processed using the APEX4 software package. The structures were solved using SHELXT and refined using SHELXL within Olex2.[25−28] All non-hydrogen atoms were refined anisotropically, while hydrogen atoms were calculated at their ideal positions and refined using a riding model with fixed U_{iso} values. For complexes **1** and **2**, there is a consistent mixed anion feature for one of the bromide anions, in the ratios of 0.8 Br^-:0.2 NO_3^- (**1**) and 0.6 Br^-:0.4 NO_3^- (**2**). Complex **3** has two spatially disordered bromides, each split (4:1) across two nearby positions. Occupancies were determined using a free variable to ensure the two parts had occupancies summing to one, before rounding the occupancy of each part appropriately. Also present in complex **3** is a spatially disordered solvent molecule (methanol), which sits adjacent to one of the spatially disordered bromide anions in a 0.8 (MeOH):0.2 Br^- ratio. Complex **4** has a spatially disordered bromide (17:3) split across two nearby positions. Occupancies were determined by using a free variable and rounded appropriately. For complex **5**, each nitrate and chloride anion share occupancy at a 0.5:0.5 ratio and are located approximately at the same central position. The ether solvate also has half occupancy, as determined by the free refinement of its occupancy. For complex **6**, a partial occupancy noncoordinated MeOH solvent molecule is present. The occupancy was determined by first allowing free refinement and then rounded to 0.75. For complex **7**, the unit cell contains a half occupancy chloride (note that Z' = 0.5; therefore, the complex contains an integer number of chlorides by symmetry $\left(\frac{3}{2} - x, +y, 1 - z\right)$), which is spatially disordered in the ratio (37:13). Occupancies were determined using a free variable and then rounded appropriately. For complexes **5**, **6**, and **8**, the data quality is poor and as such these structures should be considered as an indication of connectivity only.

For complexes **3**−**8**, a solvent mask, as implemented in Olex2, was used to account for the electron density of diffuse or disordered solvent molecules.[29] Details are as follows:

3: A solvent mask was calculated, and 72 electrons were found in a volume of 184 Å^3 in one void per unit cell. This is consistent with the presence of one MeOH (18 electrons) per asymmetric unit (Z' = 1), which accounts for 72 electrons per unit cell (Z = 4).

4: A solvent mask was calculated, and 64 electrons were found in a volume of 202 Å^3 in one void per unit cell. This is consistent with the presence of one MeOH (18 electrons) per asymmetric unit (Z' = 1), which accounts for 72 electrons per unit cell (Z = 4).

5: A solvent mask was calculated, and 142 electrons were found in a volume of 520 Å^3 in one void per unit cell. This is consistent with the presence of two MeOH (18 electrons) per asymmetric unit (Z' = 1), which accounts for 144 electrons per unit cell (Z = 4).

6: A solvent mask was calculated, and 667 electrons were found in a volume of 2169 Å^3 in one void per unit cell. This is consistent with the presence of seven MeOH (18 electrons) and one Et_2O (42 electrons) per asymmetric unit (Z' = 0.5), which accounts for 672 electrons per unit cell (Z = 4).

7: A solvent mask was calculated, and 622 electrons were found in a volume of 2687 Å^3 in one void per unit cell. This is consistent with the presence of six MeOH (18 electrons) and one Et_2O (42 electrons) per asymmetric unit (Z' = 0.5), which accounts for 600 electrons per unit cell (Z = 4).

8: A solvent mask was calculated, and 308 electrons were found in a volume of 1056 Å^3 in one void per unit cell. This is consistent with the presence of four MeOH (18 electrons) per asymmetric unit (Z' = 0.5), which accounts for 288 electrons per unit cell (Z = 4).

Magnetic Measurements. Magnetic measurements were conducted at The University of Electro-Communications, Tokyo, Japan. The DC and AC magnetic susceptibilities were measured on a Quantum Design MPMS3 SQUID magnetometer. The susceptibility data were acquired at 500 Oe in a temperature range from 1.8 to 300 K. The magnetization was recorded at 0−7 T and 1.8 K. To avoid a torquing effect, the specimens were fixed with a small amount of eicosane. The magnetic responses were corrected with diamagnetic blank data of a gelatin capsule sample holder and eicosane matrix, measured separately, and further diamagnetic contributions were estimated from Pascal's constants.[25−28] The AC susceptibility was recorded with frequencies from 1 Hz to 1 kHz, and the temperature dependence was measured on a heating mode. Note: CHN data show good agreement

https://doi.org/10.1021/acsomega.5c01224
ACS Omega 2025, 10, 50839−50849

Scheme 1. General Complexation Reaction Undertaken by Complexes 1−8

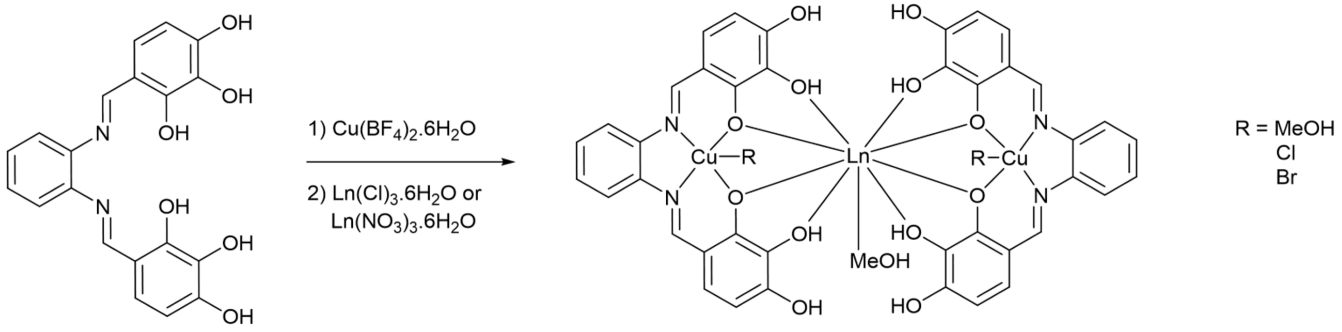

between the bulk samples and the chemical composition of the single crystals used in X-ray analysis. Samples sent for CHN and magnetic analyses were procured from the same bulk material and subjected to identical packing procedures. The complex formulations agree across different batches as determined by CHN analyses and on repeated X-ray checks; therefore, we are confident that their stoichiometries remain consistent across crystals from different batches and in the bulk sample for magnetic analysis.

SYNTHETIC METHODS

2,3,4-Trihydroxybenzaldehyde. Adapted from the procedure of Zelazkova and Jampilek, anhydrous $AlCl_3$ (21.15 g, 0.158 mol, 2 equiv) was dissolved in EtOAc (330 mL) under argon.[30] After cooling the mixture to 0 °C, pyrogallol (10.01 g, 0.079 mol, 1 equiv) and $HC(OEt)_3$ (39.6 mL, 0.238 mol, 3 equiv) were added and stirred for 30 min at 0 °C resulting in a bright-red solution. Cold aqueous HCl (10%, 100 mL) was added to the reaction mixture. The aqueous layer was separated and washed with Et_2O (3 × 120 mL), and the combined organic layers were washed with brine (5 × 100 mL), dried over anhydrous $MgSO_4$, filtered, and concentrated *in vacuo* to afford **8** as light-beige crystals (8.03 g, 0.052 mol, 66%). MP: 150−152 °C. The ^{1}H NMR spectrum agreed with the literature values (500 MHz, $CDCl_3$): δ 11.39 (1H, s, Ar−O**H**), 9.71 (1H, s, O = C**H**), 7.10 (1H, d, J = 8.6 Hz, Ar-**H**), 6.63 (1H, d, J = 8.6 Hz, Ar-**H**), 6.21 (1H, s, Ar−O**H**), 5.78 (1H, s, Ar−O**H**) ppm.[31]

*N,N′-Bis(2,3,4-trihydroxybenzylidene)-1,2-phenylenediamine (**H$_6$L**).* A solution of 2,3,4-trihydroxybenzaldehyde (0.62 g, 4.02 mmol, 2 equiv) in anhydrous MeOH (5 mL) was added dropwise to a stirred solution of 1,2-phenylenediamine (0.22 g, 2.03 mmol, 1 equiv) in anhydrous MeOH (5 mL). The resulting mixture was heated to reflux at 70 °C for 4 h, cooled to room temperature, and concentrated *in vacuo*. To the resulting solid was added MeOH (3 mL) and Et_2O (100 mL) and sonicated for 1 min. The precipitate was collected by vacuum filtration and washed with Et_2O (60 mL) to afford **H$_6$L** as a bright-orange solid (0.67 g, 1.76 mmol, 88%). MP: 216−219 °C. The ^{1}H NMR spectrum agreed with the literature values (500 MHz, DMSO-d_6): δ 13.29 (2H, bs, Ar−O**H**), 9.73 (2H, bs, Ar−O**H**), 8.73 (2H, s, N = C−**H**), 8.55 (2H, bs, Ar−O**H**)), 7.32−7.39 (4H, m, Ar−**H**) 6.98 (2H, d, J = 8.6 Hz, Ar−**H**), 6.42 (2H, d, J = 8.5 Hz, Ar−**H**) ppm.[32]

*General Synthetic Procedure for Complexes **1**−**8** (Scheme 1).* A solution of $Cu(BF_4)_2{\cdot}H_2O$ (0.02 g, 0.078 mmol) in MeOH (5 mL) was added to a stirred solution of **H$_6$L** (0.03 g, 0.079 mmol) in MeOH (5 mL) and heated to 50 °C for 30 min. A solution of $Ln(NO_3)_3{\cdot}6H_2O$ (**1**, **2**, **5**, and **6**) or $LnCl_3{\cdot}6H_2O$ (**3**, **4**, **7**, and **8**) (0.05 mmol) in MeOH (5 mL) was added followed by addition of tetrabutylammonium bromide (0.15 g, 0.47 mmol) (**1**−**4**) or tetrabutylammonium chloride (0.12 g, 0.43 mmol) (**5**−**8**). The solution was then stirred for a further 2 h at 50 °C before filtering. Vapor diffusion of Et_2O into the filtrate over 2 weeks afforded crystals suitable for X-ray diffraction.

To obtain the requisite amount of material for magnetic analysis, an alternative synthetic method was developed.

*General Synthetic Procedure for Bulk Quantities of Complexes **1**−**4**.* A solution of $CuBr_2$ (0.18 g, 0.806 mmol) in MeOH (25 mL) was added to a stirred solution of **H$_6$L** (0.30 g, 0.0789 mmol) in MeOH (25 mL) and heated to 50 °C for 30 min. A solution of $LnCl_3{\cdot}6H_2O$ or $Ln(NO_3)_3{\cdot}6H_2O$ (0.60 mmol) in MeOH (25 mL) was added and stirred for a further 30 min. Et_2O was added until a precipitate formed. The precipitate was filtered and then washed with a 5:95 mixture of MeOH:Et_2O (3 × 50 mL) followed by a Soxhlet extraction with Et_2O for 72 h, which washed out the remaining impurities. The precipitate was recovered and dried under reduced pressure yielding the desired products as a solid.

*General Synthetic Procedure for Bulk Quantities of Complexes **5**−**8**.* A solution of $CuCl_2$ (0.11 g, 0.818 mmol) in MeOH (5 mL) was added to a stirred solution of **H$_6$L** (0.30 g, 0.789 mmol) in MeOH (25 mL) and heated to 50 °C for 30 min. A solution of $LnCl_3{\cdot}6H_2O$ or $Ln(NO_3)_3{\cdot}6H_2O$ (0.60 mmol) in MeOH (25 mL) was added and stirred for a further 30 min. Et_2O (100 mL) was added, until a precipitate formed. The precipitate was filtered and then washed with a 5:95 mixture of MeOH:Et_2O (3 × 50 mL) followed by a Soxhlet extraction with Et_2O for 72 h. The precipitate was recovered and dried under reduced pressure yielding the desired products as microcrystalline solids. Purity and chemical composition of the bulk complexes were determined through CHN elemental analysis, ATR-IR, and ESI-MS.

*1. [(H$_4$**L1**)$_2$Cu$_2$Y(MeOH)$_2$Br](MeOH)$_4$Br$_{1.8}$(Et$_2$O)(NO$_3$)$_{0.2}$.* Red needle-shaped crystals, yield 22% based on $Y(NO_3)_3{\cdot}6H_2O$. ATR-IR $\bar{\nu}$: 3140, 1602, 1581, 1558, 1498, 1463, 1384, 1344, 1281, 1187, 1087, 1005, 871, 794, 751, 722, 630, 597, 539 cm^{-1}. Elemental analysis calculated (%) for $C_{40}H_{28}N_4O_{12}Cu_2Y{\cdot}Br_3(MeOH)_6Et_2O$: C 40.61, H 4.23, N 3.79; found C 38.69, H 4.07, N 3.69. ESI-MS m/z 970.81 $[(H_3\mathbf{L1})_2Cu_2Y]^+$, 485.59 $[(H_3\mathbf{L1})(H_4\mathbf{L1})Cu_2Y]^{2+}$.

*2. [(H$_4$**L1**)$_2$Cu$_2$Gd(MeOH)$_2$Br](MeOH)$_4$Br$_{1.6}$(Et$_2$O)(NO$_3$)$_{0.4}$.* Red needle-shaped crystals, yield 38% based on $Gd(NO_3)_3{\cdot}6H_2O$. ATR-IR $\bar{\nu}$: 3131, 1626, 1602, 1557, 1553, 1538, 1495, 1456, 1436, 1386, 1279, 1185, 1086, 1001, 871, 793, 751, 720, 655, 593, 539 cm^{-1}. Elemental analysis calculated (%) for $C_{40}H_{28}N_4O_{12}Cu_2Gd{\cdot}Br_3(MeOH)_6Et_2O$: C 38.82, H 4.04, N

https://doi.org/10.1021/acsomega.5c01224
ACS Omega 2025, 10, 50839−50849

3.62; found C 38.56, H 4.18, N 3.55. ESI-MS m/z 1037.95 $[(H_3\mathbf{L1})_2Cu_2Gd]^+$, 520.16 $[(H_3\mathbf{L1})(H_4\mathbf{L1})Cu_2Gd]^{2+}$.

*3. [(H$_4$**L1**)$_2$Cu$_2$Er(MeOH)$_2$Br](MeOH)$_{3.8}$Br$_2$(Et$_2$O).* Red needle-shaped crystals, yield 44% based on $ErCl_3{\cdot}6H_2O$. ATR-IR $\overline{\nu}$: 3168, 1623, 1600, 1557, 1498, 1456, 1382, 1338, 1280, 1196, 1091, 1012, 798, 754, 723 cm^{-1}. Elemental analysis calculated (%) for $C_{40}H_{28}N_4O_{12}Cu_2Er{\cdot}Br_3(MeOH)_6Et_2O$: C 38.57, H 4.01, N 3.60; found C 38.53, H 4.24, N 3.57. ESI-MS m/z 1048.04 $[(H_3\mathbf{L1})_2Cu_2Er]^+$, 524.66 $[(H_3\mathbf{L1})(H_4\mathbf{L1})Cu_2Er]^{2+}$.

*4. [(H$_4$**L1**)$_2$Cu$_2$Tb(MeOH)$_2$Br](MeOH)$_4$Br$_2$(Et$_2$O).* Red needle-shaped crystals, yield 31% based on $TbCl_3{\cdot}6H_2O$. ATR-IR $\overline{\nu}$: 3111, 1626, 1602, 1557, 1495, 1455, 1386, 1280, 1187, 1002, 794, 751, 720 cm^{-1}. Elemental analysis calculated (%) for $C_{40}H_{28}N_4O_{12}Cu_2Tb{\cdot}Br_3(MeOH)_6Et_2O$: C 38.78, H 4.04, N 3.62; found C 38.68, H 4.18, N 3.57. ESI-MS m/z 1040.98 $[(H_3\mathbf{L1})_2Cu_2Tb]^+$, 520.72 $[(H_3\mathbf{L1})(H_4\mathbf{L1})Cu_2Tb]^{2+}$.

*5.[(H$_4$**L1**)$_2$Cu$_2$Y(MeOH)$_2$(NO$_3$)$_{0.5}$Cl$_{0.5}$](MeOH)$_3$Cl(Et$_2$O)(NO$_3$).* Red needle-shaped crystals, yield 14% based on $Y(NO_3)_3{\cdot}6H_2O$. ATR-IR $\overline{\nu}$: 3131, 1629, 1603, 1582, 1560, 1498, 1462, 1388, 1345, 1282, 1231, 1190, 1093, 1005, 872, 795, 753, 722, 658, 540, 485 cm^{-1}. Elemental analysis calculated (%) for $C_{40}H_{28}N_4O_{12}Cu_2Y{\cdot}Cl_3(MeOH)_5Et_2O$: C 42.26, H 4.19, N 4.16; found C 44.64, H 4.65, N 4.16. ESI-MS m/z 970.83 $[(H_3\mathbf{L1})_2Cu_2Y]^+$, 485.55 $[(H_3\mathbf{L1})(H_4\mathbf{L1})Cu_2Y]^{2+}$.

*6. [(H$_4$**L1**)$_2$Cu$_2$GdCl$_2$](MeOH)$_9$Cl(Et$_2$O).* Red needle-shaped crystals yield 18% based on $Gd(NO_3)_3{\cdot}6H_2O$. ATR-IR $\overline{\nu}$: 2989, 1600, 1553, 1489, 1456, 1386, 1338, 1280, 1187, 1087, 1010, 752, 720 cm^{-1}. Elemental analysis calculated (%) for $C_{40}H_{28}N_4O_{12}Cu_2Gd{\cdot}Cl_3(MeOH)_6Et_2O$: C 42.48, H 4.42, N 3.96; found C 42.16, H 4.38, N 4.02. ESI-MS m/z 1039.95 $[(H_3\mathbf{L1})_2Cu_2Gd]^+$, 520.16 $[(H_3\mathbf{L1})(H_4\mathbf{L1})Cu_2Gd]^{2+}$.

*7. [(H$_4$**L1**)$_2$Cu$_2$ErCl$_2$](MeOH)$_6$Cl(Et$_2$O).* Red plate-shaped crystals, yield 16% based on $ErCl_3{\cdot}6H_2O$. ATR-IR $\overline{\nu}$: 3164, 1628, 1604, 1562, 1499, 1461, 1387, 1346, 1283, 1232, 1190, 1093, 1006, 873, 795, 753, 723, 660, 598, 540, 485 cm^{-1}. Elemental analysis calculated (%) for $C_{40}H_{28}N_4O_{12}Cu_2Er{\cdot}Cl_3(MeOH)_6Et_2O$: C 41.18, H 4.39, N 3.94; found C 42.19, H 4.37, N 3.84. ESI-MS m/z 1047.95 $[(H_3\mathbf{L1})_2Cu_2Er]^+$, 524.66 $[(H_3\mathbf{L1})(H_4\mathbf{L1})Cu_2Er]^{2+}$.

*8. [(H$_4$**L1**)$_2$Cu$_2$Tb(H$_2$O)Cl$_2$](H$_2$O)$_2$(MeOH)$_7$Cl.* Red plate-shaped crystals, yield 27% based on $TbCl_3{\cdot}6H_2O$. ATR-IR $\overline{\nu}$: 3098, 1627, 1603, 1559, 1498, 1460, 1387, 1345, 1283, 1230, 1189, 1086, 1006, 872, 794, 722, 657, 595, 539, 503, 484 cm^{-1}. Elemental analysis calculated (%) for $C_{40}H_{28}N_4O_{12}Cu_2Tb{\cdot}Cl_3(MeOH)_6Et_2O$: C 42.43, H 4.42, N 3.96; found C 42.63, H 4.18, N 3.90. ESI-MS m/z 1040.95 $[(H_3\mathbf{L1})_2Cu_2Tb]^+$, 520.72 $[(H_3\mathbf{L1})(H_4\mathbf{L1})Cu_2Tb]^{2+}$.

RESULTS AND DISCUSSION

X-ray Structural Analysis. The bromide containing complexes **1**−**4** all crystallized in the monoclinic space group $P2_1/n$ and are essentially isostructural (see Figure 1 for a representative example). The Ln^{III} center for all four complexes is nonacoordinate, with eight sites being bound to two $\mathbf{H_4L}^{2-}$ molecules through two phenolate and two hydroxy groups per ligand with the final site occupied by a bound MeOH molecule. Each Cu^{II} center is penta-coordinate with the four equatorial binding sites occupied by two imine and two phenolate groups of $\mathbf{H_4L}^{2-}$. The final site is occupied by either one bromide anion (Cu1) or one MeOH group (Cu2) anion, affording a square-pyramidal geometry. The asymmetric units of complexes **1**−**4** contain the $\mathbf{H_4L}_2Cu_2LnBr(MeOH)_2$ unit as

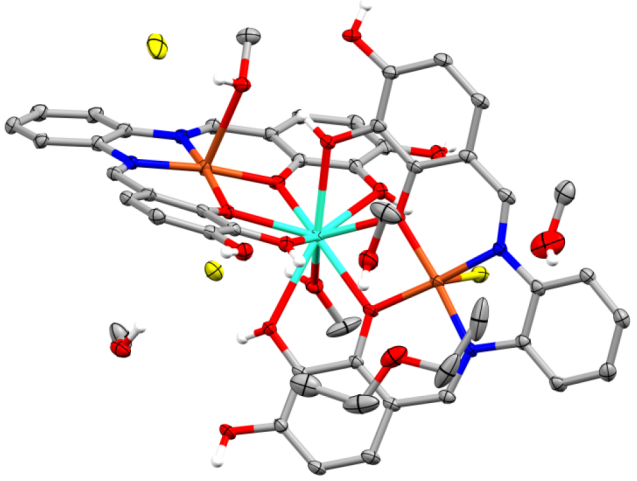

Figure 1. X-ray crystal structure of the asymmetric unit of **4**. Thermal ellipsoids are shown at the 30% probability level. Color code: C, N, O, Cu, Tb, and Br are gray, blue, red, orange, cyan, and gold, respectively. Selected hydrogen atoms have been omitted for the sake of clarity.

well as an additional four noncoordinated MeOH molecules, two bromide anions, and a single Et_2O molecule (Figure 1).

Complexes **1** and **2** have a 0.2 or 0.4 occupancy nitrate ion occupying the same space as a 0.8 or 0.6 occupancy bromide ion, respectively. Of the chloride containing complexes, **5** crystallized in the monoclinic space group $P2_1/n$, **6** in $C2/_C$, and **7** and **8** in $I2/a$. The space group $I2/a$ can be converted to $C2/_C$, with an appropriate cell choice, thus giving cell parameters quite close to those of complex **6**. The Ln^{III} centers for complexes **5** and **8** are nonacoordinate, with eight sites being bound to two $\mathbf{H_4L}^{2-}$ molecules through two phenolate and two hydroxy groups per ligand. The final site is occupied by a bound MeOH or H_2O molecule for complexes **5** and **8**, respectively. The Ln^{III} center for complexes **6** and **7** is octacoordinate with all eight sites being occupied by two $\mathbf{H_4L}^{2-}$ molecules. Each Cu^{II} center is pentacoordinate with the four equatorial binding sites occupied by two imine and two phenolate groups of $\mathbf{H_4L}$. The final site is occupied by a chloride anion, giving an overall square-pyramidal geometry. The asymmetric unit of complex **5** is the same as complexes **1**−**4** except with the bromide anions being replaced with a split of 0.5 occupancy chloride and nitrate anions. The asymmetric unit of complexes **6**−**8** each contain a $[\mathbf{H_4L}CuLn_{0.5}Cl]^{0.5}$ unit, which represents half of the overall architecture with **6** containing one well-defined MeOH molecule and a half-occupied chloride ion. Seven further MeOH molecules, and an Et_2O molecule are poorly defined. Complex **7** contains a half-occupied chloride ion spread across two sites, as well as six MeOH and one Et_2O molecule that are poorly defined. While complex **8** contains one water molecule, one and a half methanol molecules, one chloride ion, and a further four poorly defined MeOH molecules. Within the complexes, the Cu−Ln distance and the Cu−O−Ln bond angles are of particular interest as these relate to potential magnetic exchange between the metal centers (Figure 2).[33] The bromide containing complexes **1**−**4** tended to have larger Cu−Ln distances and angles than the chloride containing complexes **5**−**8** (Table 1).

Secondary Interactions. All of the complexes reported displayed intramolecular hydrogen bonding between the species bound at the apical site of the copper ions and the

https://doi.org/10.1021/acsomega.5c01224
ACS Omega 2025, 10, 50839−50849

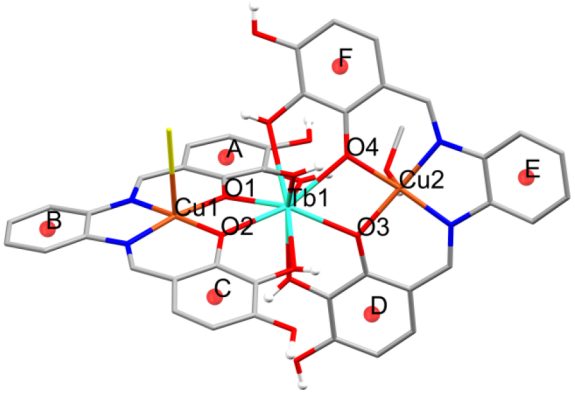

Figure 2. X-ray crystal structure of **4**. Noncoordinated species and selected hydrogen atoms have been omitted for clarity. Color code: C, N, O, Cu, Tb, and Br are gray, blue, red, orange, cyan, and gold, respectively. Atom labels for the selected bond lengths and angles reported in Table 1 are provided and are consistent for complexes **1**–**8**. Centroids used in determination of $\pi-\pi$ stacking are labeled and are consistent for all complexes.

nearest phenolic hydrogen. The bromide hydrogen bonding interactions range from 2.466(1) to 2.65(9) Å, the MeOH from 1.75(1) to 1.93(9) Å, and chloride from 2.300(2) to 2.309(4) Å, with no apparent correlation to lanthanide size (Table 2).

The size of these interactions correlates with the comparative electronegativities of the donor species, with bromide being the least electronegative, thus having the longest hydrogen bonds, while oxygen is the most electronegative and has the shortest hydrogen bonds. The bromide containing series (**1**–**4**) all possess an identical array of $\pi-\pi$ stacking interactions, with five of the six aromatic rings per unit of complex being involved in $\pi-\pi$ stacking. Each pair of dual $\pi-\pi$ stacking interactions forms a chain of alternating conformations of the linked complexes (Figure 3). Each complex possesses a single $\pi-\pi$ stacking interaction with a complex in a neighboring chain. This network of interactions result in a zigzag arrangement of the supramolecular sheets where every second unit of the complex along the chain has a single interchain $\pi-\pi$ stacking interaction while the remaining complex units have only intrachain $\pi-\pi$ stacking interactions (Figure 4). These sheets layer within the gaps in the zigzag lattice such that the intersheet Ln–Ln distance is shorter than either of the inter- or intrachain distances (Figure 5). Three distinct intermolecular hydrogen bonding interactions are observed: two interchain and the other between complex sheets. The intersheet interaction occurs between the bromide anion bound to the apical position of the copper ion and a phenolic hydrogen of a neighboring complex (Figure 6, interaction a). This interaction helps explain the relatively close intersheet distance. The first interchain interaction occurs between the MeOH group bound to the apical position of the copper ion, to an uncoordinated bromide anion, which in turn is hydrogen bonded to a noncoordinating phenol of a separate complex (Figure 6, interaction b). The final interaction is between the MeOH group bound to the lanthanide, through an uncoordinated bromide anion to a nonbinding phenol of a separate complex (Figure 6, interaction c).

Table 2. Intramolecular Hydrogen Bonding Interactions for Complexes 1–8

	1	2	3	4
Br–OH	2.65(9)	2.530(1)	2.467(1)	2.466(1)
MeOH–OH	1.93(9)	1.875(4)	1.859(5)	1.75(1)
	5	**6**	**7**	**8**
Cl–OH		2.301(3)	2.300(2)	2.309(4)

The chloride containing series (**6**–**8**) has a more extensive $\pi-\pi$ stacking network, with each of the six aromatic rings involved in $\pi-\pi$ stacking. The intrachain $\pi-\pi$ stacking interactions are analogous to those found in the bromide series, with two pairs of two $\pi-\pi$ stacking interactions linking neighboring complexes (Figure 3). The remaining two rings each have a single $\pi-\pi$ stacking with a complex in a separate chain (Figure 7). This results in a 3D supramolecular lattice with individual complexes packed much closer than those of the bromide analogues. Lists of the relevant Ln–Ln distances and $\pi-\pi$ stacking distances and angles are found in Tables S4 and S5, respectively.

Magnetic Analysis. DC magnetic susceptibility and magnetization measurements were initially taken on diamagnetic yttrium containing complexes **1** and **5** in order to assess the Cu–Cu interactions. The $\chi_m T$ products reached a maximum of 0.84 and 0.81 cm^3 K mol^{-1} at 300 K (Figure 8 top and Table 3), indicative of two isolated $S = {}^1/_2$ spins with g = 2.08 and 2.12, for complexes **1** and **5**, respectively, which agrees with the expected value of ca. 2.1.

There was virtually no change in the $\chi_m T$ plot indicating a lack of any exchange interactions between the Cu^{II} centers. The magnetization values for both complexes were nearly identical, 2.14 and 2.13 $N_A\mu_B$ at 7 T for complexes **1** and **5**, respectively, exceeding the theoretical saturation magnetization of 2.0 $N_A\mu_B$ (Figure 8 bottom). The $\chi_m T$ product for the gadolinium containing complexes **2** and **6** reached a maximum of 8.37 and 7.83 cm^3 K mol^{-1} at 300 K, respectively, which are close to the theoretical spin-only value of 8.63 cm^3 K mol^{-1}. They also exhibited a sharp increase in the $\chi_m T$ product when cooled below ca. 60 K reaching peak of 11.8 and 11.0 cm^3 K mol^{-1} at ca. 5 K for complexes **2** and **6**, respectively. Furthermore, the monotonic increase in the $\chi_m T$ values upon

Table 1. Selected Structural Parameters for Complexes 1–8

	Cu1–Ln (Å)	Cu2–Ln (Å)	Cu1–O1–Ln (°)	Cu1–O2–Ln (°)	Cu2–O1–Ln (°)	Cu2–O2–Ln (°)	ave. Cu–O–Ln (°)
1	3.397(1)	3.411(1)	108.2(2)	106.2(2)	108.0(2)	107.3(2)	107.4(2)
2	3.421(1)	3.435(1)	108.2(2)	106.2(2)	107.4(2)	107.4(2)	107.3(2)
3	3.379(1)	3.392(1)	105.8(2)	108.2(3)	107.7(2)	106.8(3)	107.1(3)
4	3.405(1)	3.421(1)	107.8(2)	105.9(2)	107.8(2)	106.9(2)	107.1(2)
5	3.363(2)	3.360(2)	105.3(3)	107.2(3)	106.0(3)	106.2(3)	106.2(3)
6	3.320(2)	3.320(2)	106.9(4)	106.7(4)	106.9(4)	106.7(4)	106.8(4)
7	3.342(1)	3.342(1)	106.6(2)	106.0(2)	106.6(2)	106.0(2)	106.3(2)
8	3.390(3)	3.390(3)	108.4(5)	106.8(5)	108.4(5)	106.8(5)	107.6(5)

https://doi.org/10.1021/acsomega.5c01224
ACS Omega 2025, 10, 50839–50849

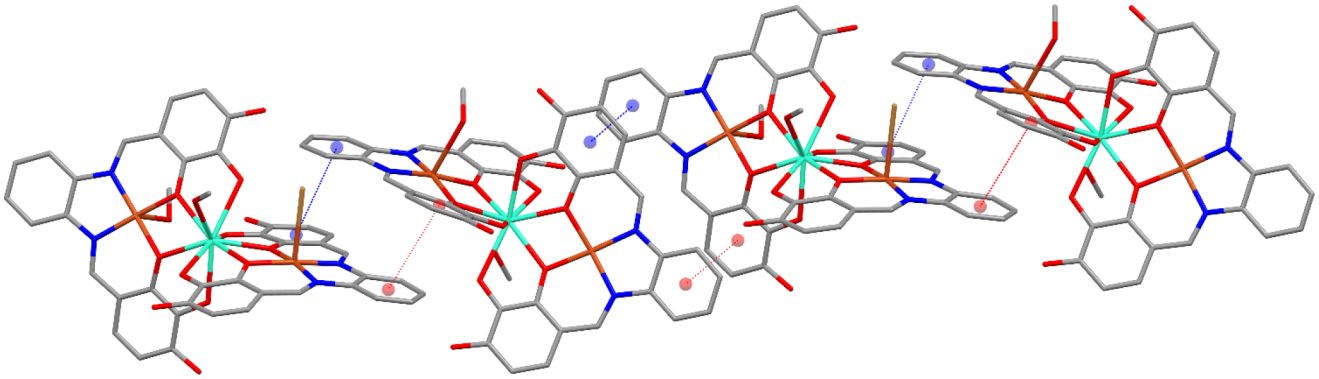

Figure 3. X-ray crystal structure of complex **4** showing the intrachain $\pi-\pi$ stacking interactions present in complexes **1**−**4**. The dashed lines represent identical interactions. Solvent molecules and hydrogen atoms were omitted for clarity.

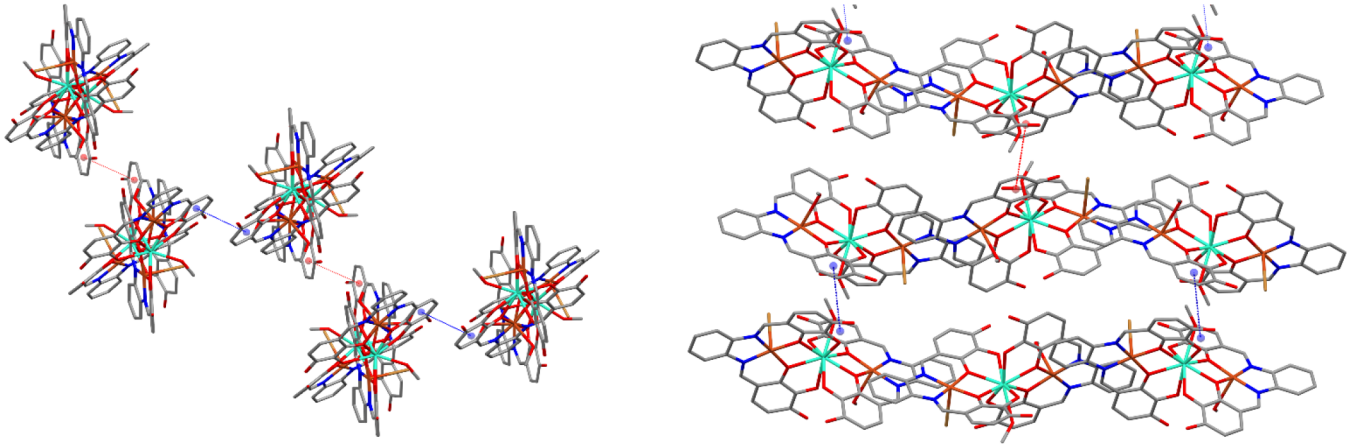

Figure 4. X-ray crystal structure of **4** showing the single $\pi-\pi$ stacking interactions viewing from down the chain (left) and at the chain (right) for complexes **1**−**4**. Solvent molecules and hydrogen atoms have been omitted for clarity.

cooling is also indicative of the presence of ferromagnetic exchange interactions. The exchange model is $\mathcal{H} = -2J(\hat{S}_{Cu1} \times \hat{S}_{Gd} + \hat{S}_{Gd} \times \hat{S}_{Cu2})$, and the following van Vleck equation was given:

$$\chi_m T = \frac{N_A \mu_B g^2}{3k_B T} \times \frac{165 + 84\exp\left(-\frac{9J}{k_B T}\right) + 35\exp\left(-\frac{16J}{k_B T}\right) + 84\exp\left(-\frac{7J}{k_B T}\right)}{5 + 4\exp\left(-\frac{9J}{k_B T}\right) + 3\exp\left(-\frac{16J}{k_B T}\right) + 4\exp\left(-\frac{7J}{k_B T}\right)} \times a$$

Here, $2J$ implies the exchange coupling constant, and the purity factor is confined to a. The parameters were optimized as $2J/k_B$ = 12.18(12) and 11.6(2) K and a = 0.9428(7) and 0.8940(12) for **2** and **6**, respectively. The curves calculated from the van Vleck equation matched the experimental data (Figure 8 top). The magnetization measurements for complexes **2** and **6** reached a maximum of 8.95 and 9.06 $N_A\mu_B$ at 7 T, respectively, which approximately coincide with the theoretical saturation magnetization (Figure 8 bottom). An anomaly was recorded in the AC magnetic susceptibility measurements for complex **2** at an applied 2000 Oe DC field below ca. 5 K (Figure S1).

The $\chi_m T$ product for the erbium containing complexes **3** and **7** (Figure 9 top) reached a maximum of 11.77 and 12.20 cm^3 K mol^{-1} at 300 K, respectively, which nears the theoretical value of 12.30 cm^3 K mol^{-1}. The $\chi_m T$ plot for **3** and **7** shows a monotonic decrease upon cooling to ca. 5 K indicative of weak antiferromagnetic coupling and/or crystal-field splitting of the Er^{III} ion.[34] Below this temperature, the $\chi_m T$ value for **3** sharply increases, owing to ferromagnetic exchange coupling between the Er^{III} and Cu^{II}. On the other hand, the $\chi_m T$ plot for **7** shows a monotonic decrease upon cooling, indicating that any possible Er−Cu ferromagnetic exchange coupling would be negligible. The magnetization values at 7 T were 6.80 and 7.11 $N_A\mu_B$ for **3** and **7**, respectively, which are ca. 61 and 63% the theoretical spin-only value of 11.2 $N_A\mu_B$ (Figure 9 bottom). The lower-than-expected magnetization value is likely due to the magnetic anisotropy of the erbium ion.

The bromide containing terbium complex **4** has an experimental $\chi_m T$ value of 14.13 cm^3 K mol^{-1} at 300 K, which is greater than the theoretical value of 12.64 cm^3 K mol^{-1}. The crystal structure analysis revealed that **4** contains Et_2O and MeOH as crystalline solvent molecules. These are volatile and may cause errors in weighing. The chloride containing terbium complex **8** has an experimental $\chi_m T$ value of 12.81 cm^3 K mol^{-1} at 300 K, which is in good agreement with the theoretical value. The $\chi_m T$ values of both **4** and **8** monotonically increase upon cooling until ca. 40 K where a sharp increase is observed, which is indicative of ferromagnetic coupling (Figure 9 top). A decrease in the $\chi_m T$ value is observed below ca. 10 K, which is attributed to the crystal-field splitting of the terbium ions. The magnetization value at 7 T

https://doi.org/10.1021/acsomega.5c01224
ACS Omega 2025, 10, 50839−50849

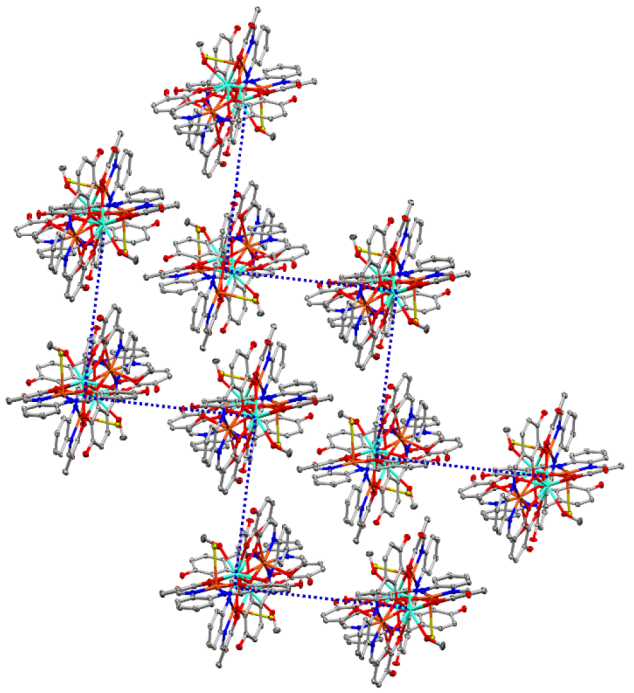

Figure 5. X-ray crystal structure showing the intersheet packing of complexes **1**−**4** viewed along the chains. Blue dashed lines indicate interchain $\pi-\pi$ stacking. Solvent molecules and hydrogen atoms have been omitted for clarity.

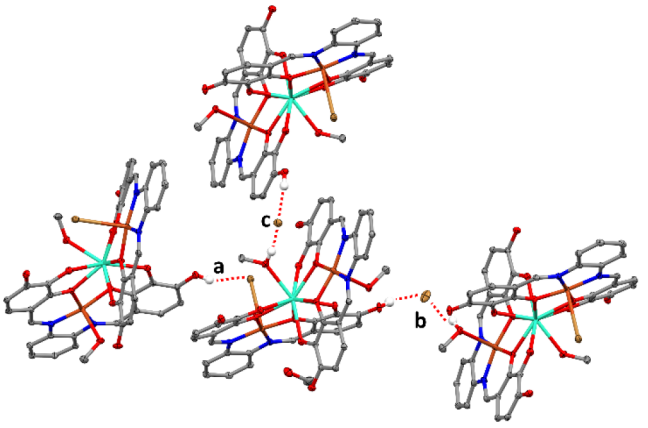

Figure 6. X-ray crystal structure showing the intermolecular hydrogen bonding interactions present in complexes **1**−**4**. Non interacting hydrogens and solvent species have been omitted for the sake of clarity.

was 7.12 and 6.94 $N_A\mu_B$ for complexes **4** and **8**, respectively, which are ca. 64 and 62% the theoretical spin-only value of 11.2 $N_A\mu_B$ (Figure 9 bottom), which is likely due to the magnetic anisotropy of the terbium ion.

AC susceptibility measurements were performed for all Gd, Tb, and Er derivatives (Figure S1). Complexes **4** and **8** exhibited features typical of SMMs such as an onset of out-of-phase AC susceptibility without any bias DC field (Figure 10 left and Figure 11 left). The frequency dependence was much clearer under an applied 1000 or 2000 Oe DC field at temperatures below ca. 5 K (Figure 10 right and Figure 11 right, and Figure S1). This is indicative of the blocking of magnetization due to an anisotropy barrier. The shift of the maximum in the χ_m'' product was observed upon application of

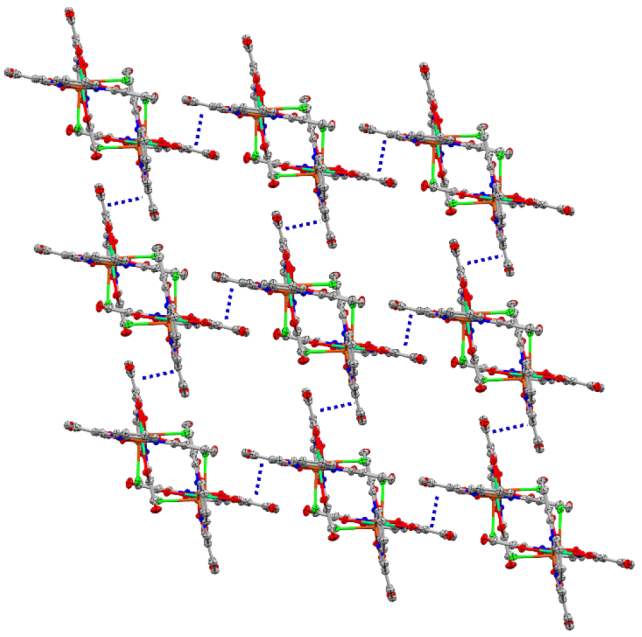

Figure 7. X-ray crystal structure showing the crystal packing for complexes **5**−**8** viewed along the chains. Blue dashed lines indicate interchain $\pi-\pi$ stacking. Solvent molecules and hydrogen atoms have been omitted for clarity.

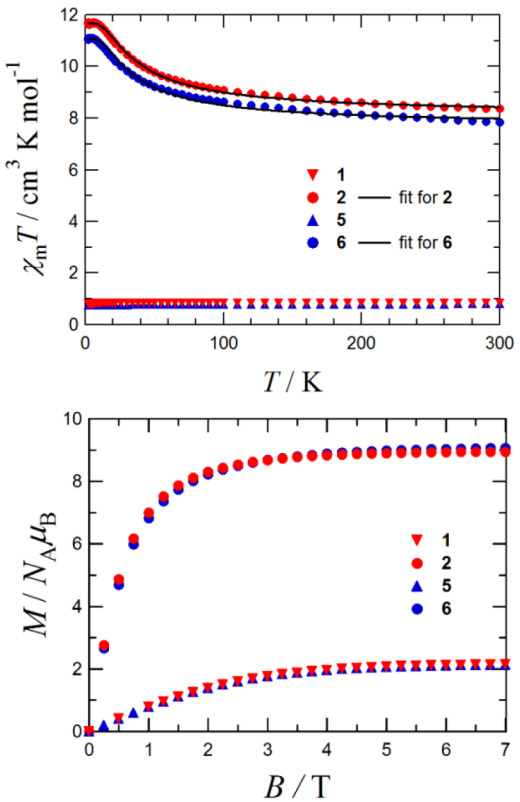

Figure 8. Superpositions of the $\chi_m T-T$ (500 Oe, top) and $M-H$ (1.8 K, bottom) curves for complexes **1**, **2**, **5**, and **6**. A solid line indicates the best fit calculated from the van Vleck equation (see the main text).

a 1000 Oe DC field, which is indicative of suppression of QTM. QTM is common in terbium complexes due to the non-Kramers nature of the terbium ion.[35] The effective barrier, U_{eff}, for **4** and **8** was calculated for the zero-DC field data using a

https://doi.org/10.1021/acsomega.5c01224
ACS Omega 2025, 10, 50839−50849

Table 3. DC Magnetic Susceptibility and Magnetization Data for Complexes 1−8

	$\chi_m T$ cm^3 K mol^{-1} (exp. at 300 K)	$\chi_m T$ (calc.)	$M/N_A\mu_B$ (exp. at 7 T)	M (calc.)
1	0.84	0.75	2.14	2
2	8.37	8.63	8.95	9
3	11.77	12.30	6.80	11.2
4	14.13	12.64	7.12	11.2
5	0.81	0.75	2.13	2
6	7.83	8.63	9.06	9
7	12.23	12.30	7.11	11.2
8	12.81	12.64	6.94	11.2

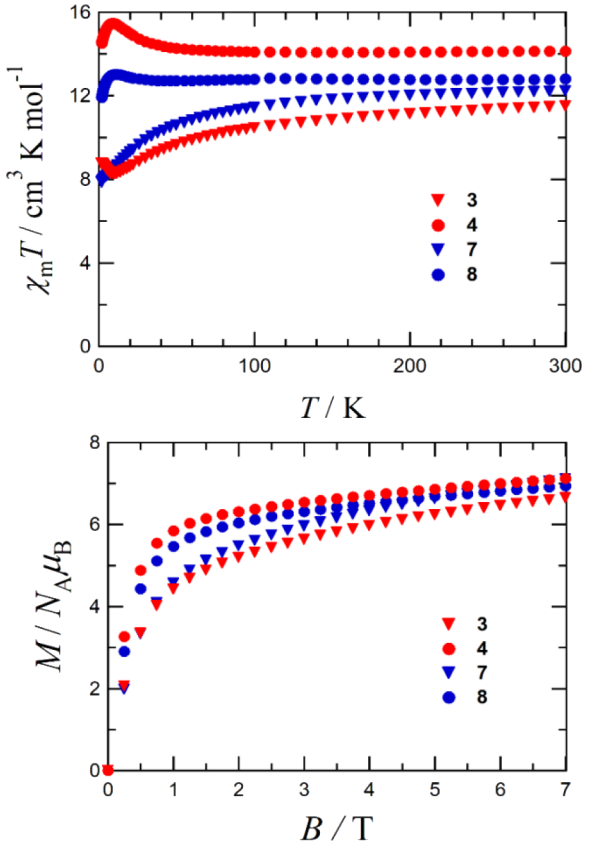

Figure 9. Superpositions of the $\chi_m T-T$ (500 Oe, top) and $M-H$ (1.8 K, bottom) curves for complexes **3** (blue) and **4** (red).

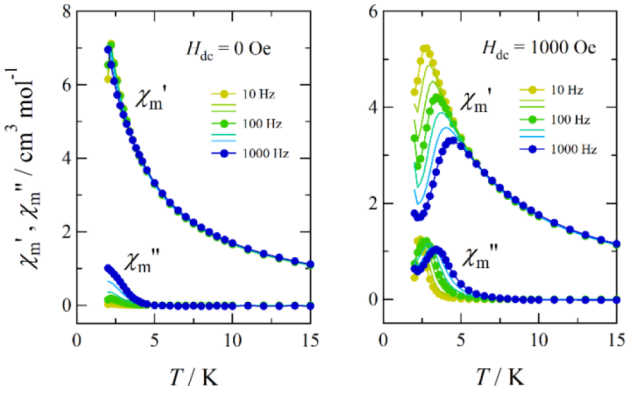

Figure 10. In-phase (χ') and out-of-phase (χ'') AC magnetic susceptibilities as a function of temperature and DC bias field (0 Oe, left, and 1000 Oe, right) for **4**.

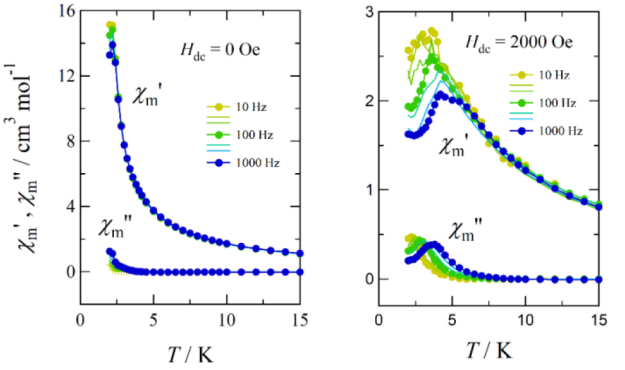

Figure 11. In-phase (χ') and out-of-phase (χ'') AC magnetic susceptibilities as a function of temperature and DC bias field (0 Oe, left; 2000 Oe, right) for **8**.

modified Arrhenius plot (Figures 12a and 13a, respectively).[36] These values are 17.8(6) and 16.0(9) K with pre-exponential

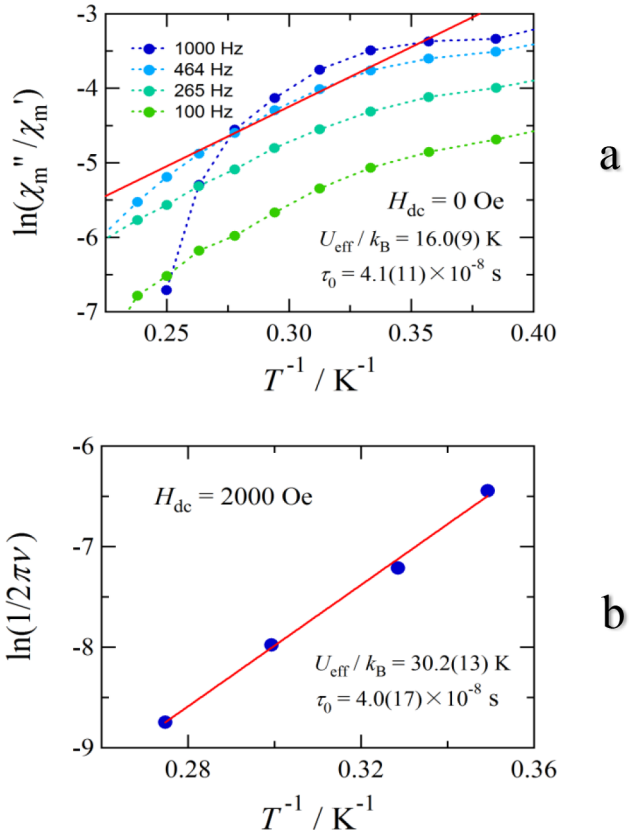

Figure 12. (a) Modified Arrhenius plot of **8**, measured at zero bias field (b) Arrhenius plot of **8**, measured at 2000 Oe bias field.

factors (τ_0) of 3.0(5) × 10^{-8} and 4.1(11) × 10^{-8} s for **4** and **8**, respectively. Additionally, according to the Arrhenius analysis (Figures 12b and 13b), the U_{eff} values measured at applied fields of 1000 Oe for **4** and 2000 Oe for **8** are 32.3(12) and 30.2(13) K with τ_0 values of 1.1(5) × 10^{-8} and 4.0(17) × 10^{-8} s, respectively. Based on the AC susceptibility data for **4** in a 1000 Oe applied field, a Cole−Cole plot can be drawn to show the relationship between in-phase (χ') and out-of-phase (χ'') data (Figure S2a).[37] The best-fit semicircular lines were given for 3.0−3.6 K. The obtained distribution index α, which is related to the distribution of relaxation times, is in the range

https://doi.org/10.1021/acsomega.5c01224
ACS Omega 2025, 10, 50839−50849

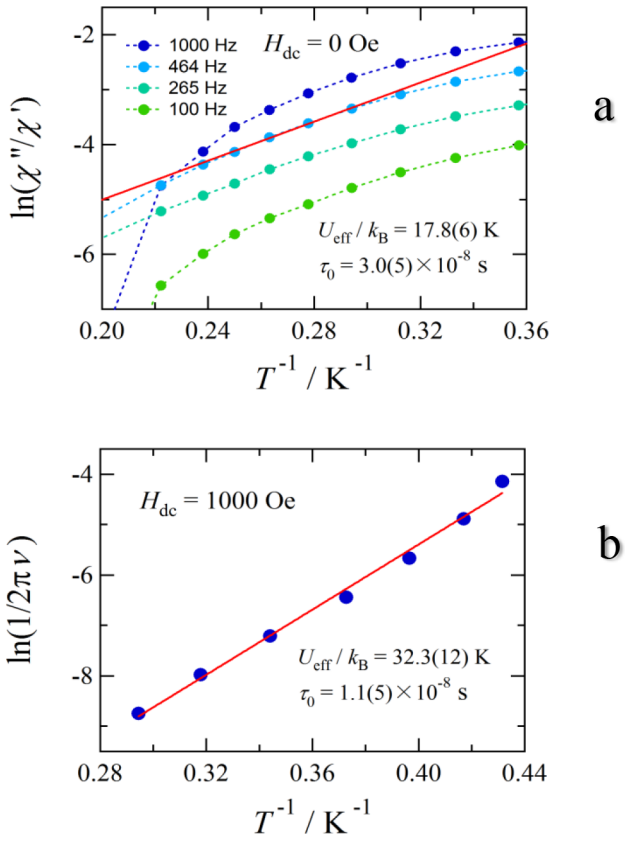

Figure 13. (a) Modified Arrhenius plot for the data of **4**, acquired at zero bias field. (b) Arrhenius plot for the data of **4**, acquired in a bias field of 1000 Oe.

0.28−0.37, inversely proportional to temperature (Table S6). The relatively low values of α indicate the likely presence of only a single relaxation mechanism possessing a broad range of relaxation times. A Cole−Cole plot for complex **8** could not be drawn as the data was too scattered (Figure S2b). A weaker DC bias field resulted in a less significant increase in χ_m'' and weaker frequency dependence. The ac susceptibility data of compound **4** at zero bias (Figure 10, left) and compound **8** with a 1000 Oe bias (Figure S1f) were subjected to a data analysis procedure similar to that used in Figures 12 and 13, but relatively large errors were obtained, as shown in Figures S3 and S4.

CONCLUSIONS

In this work, eight new complexes of the form L_2Cu_2Ln have been successfully synthesized and characterized using X-ray and magnetic analyses. These complexes fall into one of two series depending on the type of anion present, chloride, or bromide. X-ray analysis revealed that the Cu−Ln bond distances decreased with the decreasing size of the lanthanide as well as the smaller size of the anion. Further analysis showed that the intramolecular hydrogen bonding interactions do not significantly alter the Cu−Ln distance, with the hydrogen bonding distances increasing from MeOH < Cl < Br, while the Cu−Ln distance increases from Cl < Br < MeOH. Additionally, it appears that the difference in hydrogen bonding interactions between the chloride and bromide analogues does not have a significant effect on the overall supramolecular structure of the complexes. Analysis of the supramolecular structures revealed that the bromide containing complexes, **1**−**4**, have five of the six aromatic rings involved in $\pi-\pi$ stacking, forming layers of 2D sheets. The chloride containing complexes, **6**−**8**, have all aromatic rings involved in $\pi-\pi$ stacking interactions, forming an interconnected 3D supramolecular structure. This, combined with the smaller size of the chloride anion, results in a decrease in the smallest intercomplex Ln−Ln distance.

DC magnetic susceptibility measurements of the yttrium containing complexes (**1** and **5**) revealed no magnetic interaction between the two copper centers, suggesting that all magnetic activity is either entirely due to the lanthanide ion or copper-lanthanide coupling. Further analysis revealed that the erbium containing complexes **3** and **7** exhibited weak antiferromagnetic coupling between the copper and erbium ions and/or crystal-field splitting of the erbium ion. Below ca. 10 K, the bromide containing complex **3** showed possible ferromagnetic exchange coupling while the chloride containing complex **7** did not. The gadolinium and terbium containing complexes (**2**, **7** and **4**, **8**, respectively) both exhibited ferromagnetic coupling with a sharp uptick in susceptibility below ca. 50 K. AC magnetic susceptibility measurements revealed that complexes **4** and **8** exhibited zero-field SMM behavior with U_{eff} values of 17.8(6) and 16.0(9) K, respectively. The presence of QTM was identified by the shift in the χ_m'' maximum in the presence of an applied 1000 or 2000 Oe DC field. A Cole−Cole plot was able to be drawn for bromide containing complex **4**, suggesting the presence of a single relaxation mechanism. Overall, it appears that the steric effects of the bulkier bromide anion reduce the total number of $\pi-\pi$ stacking interactions. This leads to a switch from a 3D supramolecular architecture to a 2D one, which helped to more effectively isolate the magnetic centers of the complexes, enhancing the resultant magnetic properties. This shows that careful modulation of anions can lead to or enhance SMM behavior.

ASSOCIATED CONTENT

Supporting Information

The Supporting Information is available free of charge at https://pubs.acs.org/doi/10.1021/acsomega.5c01224.

Crystal structure and refinement details for **1**−**8**; selected geometrical parameters for **1**−**8**; AC magnetic susceptibility data for **2**, **3**, **4**, **6**, **7**, and **8**; Cole−Cole plots and parameters for **4** and **8**; Cole−Cole parameters for **4**; generalized Debye model fitting for **4** and **8**; and Arrhenius analysis for **4** and **8** (PDF)

Crystallographic data (CIF)

Crystallographic data (CIF)

Crystallographic data (CIF)

Crystallographic data (CIF)

Crystallographic data (CIF)

Crystallographic data (CIF)

Crystallographic data (CIF)

Crystallographic data (CIF)

AUTHOR INFORMATION

Corresponding Author

Paul G. Plieger − *School of Food Technology and Natural Sciences, Massey University, Palmerston North 4410, New Zealand;* Present Address: Fonterra Research and Development Center, Private Bag 11029, Dairy Farm

https://doi.org/10.1021/acsomega.5c01224
ACS Omega 2025, 10, 50839−50849

Road, Palmerston North, New Zealand;
Email: p.g.plieger@massey.ac.nz

Authors

Brodie E. Matheson − *School of Food Technology and Natural Sciences, Massey University, Palmerston North 4410, New Zealand*

Tyson N. Dais − *School of Food Technology and Natural Sciences, Massey University, Palmerston North 4410, New Zealand;* orcid.org/0000-0003-0781-996X

Marryllyn E. Donaldson − *School of Food Technology and Natural Sciences, Massey University, Palmerston North 4410, New Zealand*

Shin-ichiro Takeshi − *Department of Engineering Science, Graduate School of Informatics and Engineering, The University of Electro-Communication, Chofu, Tokyo 182-8585, Japan*

Liangcheng Lyu − *Department of Engineering Science, Graduate School of Informatics and Engineering, The University of Electro-Communication, Chofu, Tokyo 182-8585, Japan*

Rina Takano − *Department of Engineering Science, Graduate School of Informatics and Engineering, The University of Electro-Communication, Chofu, Tokyo 182-8585, Japan*

Takayuki Ishida − *Department of Engineering Science, Graduate School of Informatics and Engineering, The University of Electro-Communication, Chofu, Tokyo 182-8585, Japan;* orcid.org/0000-0001-9088-2526

Gareth J. Rowlands − *School of Food Technology and Natural Sciences, Massey University, Palmerston North 4410, New Zealand;* Present Address: Fonterra Research and Development Center, Private Bag 11029, Dairy Farm Road, Palmerston North, New Zealand; orcid.org/0000-0002-8661-5860

Complete contact information is available at: https://pubs.acs.org/10.1021/acsomega.5c01224

Notes

The authors declare no competing financial interest.

■ ACKNOWLEDGMENTS

The authors wish to thank Massey University for its financial support to BEM and MED (PhD scholarships) and the Massey University REaDI Iwi fund award to TND for APC fees. T.I. is grateful to the support from JSPS KAKENHI (JP20K21170 and JP17H06371).

■ REFERENCES

(1) Osa, S.; Kido, T.; Matsumoto, N.; Re, N.; Pochaba, A.; Mrozinski, J. A Tetranuclear 3d−4f Single Molecule Magnet: $[Cu^{II}LTb^{III}(hfac)_2]_2$. *J. Am. Chem. Soc.* **2004**, *126*, 420−421.

(2) Rosado Piquer, L.; Sanudo, E. C. Heterometallic 3d-4f single-molecule magnets. *Dalton. Trans.* **2015**, *44*, 8771−8780.

(3) Wernsdorfer, W.; Aliaga-Alcalde, N.; Hendrickson, D. N.; Christou, G. Exchange-biased quantum tunnelling in a supramolecular dimer of single-molecule magnets. *Nature* **2002**, *416*, 406−409.

(4) Langley, S. K.; Wielechowski, D. P.; Vieru, V.; Chilton, N. F.; Moubaraki, B.; Abrahams, B. F.; Chibotaru, L. F.; Murray, K. S. A $\{Cr_2^{III}Dy_2^{III}\}$ Single-Molecule Magnet: Enhancing the Blocking Temperature through 3d Magnetic Exchange. *Angew. Chem., Int. Ed.* **2013**, *52*, 12014−12019.

(5) Langley, S. K.; Le, C.; Ungur, L.; Moubaraki, B.; Abrahams, B. F.; Chibotaru, L. F.; Murray, K. S. Heterometallic 3d−4f Single-Molecule Magnets: Ligand and Metal Ion Influences on the Magnetic Relaxation. *Inorg. Chem.* **2015**, *54*, 3631−3642.

(6) Moreno Pineda, E.; Chilton, N. F.; Tuna, F.; Winpenny, R. E. P.; McInnes, E. J. L. Systematic Study of a Family of Butterfly-Like $\{M_2Ln_2\}$ Molecular Magnets (M = Mg^{II}, Mn^{III}, Co^{II}, Ni^{II}, and Cu^{II}; Ln = Y^{III}, Gd^{III}, Tb^{III}, Dy^{III}, Ho^{III}, and Er^{III}). *Inorg. Chem.* **2015**, *54*, 5930−5941.

(7) Matheson, B. E.; Dais, T. N.; Donaldson, M. E.; Rowlands, G. J.; Plieger, P. G. The importance of second sphere interactions on single molecule magnet performance. *Inorg. Chem. Front.* **2023**, *10*, 6427−6439.

(8) Canaj, A. B.; Singh, M. K.; Wilson, C.; Rajaraman, G.; Murrie, M. Chemical and *in silico* tuning of the magnetisation reversal barrier in pentagonal bipyramidal $Dy^{(III)}$ single-ion magnets. *Chem. Commun.* **2018**, *54*, 8273−8276.

(9) Gil, Y.; Llanos, L.; Cancino, P.; Fuentealba, P.; Vega, A.; Spodine, E.; Aravena, D. Effect of Second-Sphere Interactions on the Magnetic Anisotropy of Lanthanide Single-Molecule Magnets: Electrostatic Interactions and Supramolecular Contacts. *J. Phys. Chem. C* **2020**, *124*, 5308−5320.

(10) Gregson, M.; Chilton, N. F.; Ariciu, A.-M.; Tuna, F.; Crowe, I. F.; Lewis, W.; Blake, A. J.; Collison, D.; McInnes, E. J. L.; Winpenny, R. E. P.; Liddle, S. T. A monometallic lanthanide bis(methanediide) single molecule magnet with a large energy barrier and complex spin relaxation behaviour. *Chem. Sci.* **2016**, *7*, 155−165.

(11) Liu, X.-W.; Wu, Z.; Chen, J.-T.; Li, L.; Chen, P.; Sun, W.-B. Regulating the single-molecule magnetic properties of phenol oxygen-bridged binuclear lanthanide complexes through the electronic and spatial effect of the substituents. *Inorg. Chem. Front.* **2020**, *7*, 1229−1238.

(12) Costes, J.-P.; Donnadieu, B.; Gheorghe, R.; Novitchi, G.; Tuchagues, J.-P.; Vendier, L. Di- or Trinuclear 3d−4f Schiff Base Complexes: The Role of Anions. *Eur. J. Inorg. Chem.* **2008**, *2008*, 5235−5244.

(13) Herchel, R.; Zoufalý, P.; Nemec, I. The effect of the second coordination sphere on the magnetism of $[Ln(NO_3)_3(H_2O)_3]\cdot$(18-crown-6) (Ln = Dy and Er). *RSC Adv.* **2019**, *9*, 569−575.

(14) Lin, S.-Y.; Guo, Y.-N.; Guo, Y.; Zhao, L.; Zhang, P.; Ke, H.; Tang, J. Macrocyclic ligand encapsulating dysprosium triangles: axial ligands perturbed magnetic dynamics. *Chem. Commun.* **2012**, *48*, 6924−6926.

(15) Liu, X.; Zhao, C.; Wu, J.; Zhu, Z.; Tang, J. Air-stable chiral double-decker $Dy^{(III)}$ macrocycles with fluoride ion as the sole axial ligand. *Dalton. Trans.* **2022**, *51*, 16444−16447.

(16) Lin, S.-Y.; Wang, C.; Zhao, L.; Wu, J.; Tang, J. Chiral mononuclear lanthanide complexes and the field-induced single-ion magnet behaviour of a Dy analogue. *Dalton. Trans.* **2015**, *44*, 223−229.

(17) Liu, S.; Gil, Y.; Zhao, C.; Wu, J.; Zhu, Z.; Li, X.-L.; Aravena, D.; Tang, J. A conjugated Schiff-base macrocycle weakens the transverse crystal field of air-stable dysprosium single-molecule magnets. *Inorg. Chem. Front.* **2022**, *9*, 4982−4989.

(18) Zhu, Z.; Zhao, C.; Feng, T.; Liu, X.; Ying, X.; Li, X.-L.; Zhang, Y.-Q.; Tang, J. Air-Stable Chiral Single-Molecule Magnets with Record Anisotropy Barrier Exceeding 1800 K. *J. Am. Chem. Soc.* **2021**, *143*, 10077−10082.

(19) Song, F.-Q.; Cheng, H.; Zhao, N.-N.; Song, X.-Q.; Wang, L. Anion-Dependent Structure and Luminescence Diversity in Zn^{II}-Ln^{III} Heterometallic Architectures Supported by a Salicylamide-Imine Ligand. *Inorg. Chem.* **2021**, *60*, 17051−17062.

(20) Yang, F.; Zhou, Q.; Zeng, G.; Li, G.; Gao, L.; Shi, Z.; Feng, S. Anion effects on the structures and magnetic properties of binuclear lanthanide single-molecule magnets. *Dalton. Trans.* **2014**, *43*, 1238−1245.

(21) Mandal, L.; Biswas, S.; Cosquer, G.; Shen, Y.; Yamashita, M. Anion-driven structures and SMM behavior of dinuclear terbium and ytterbium complexes. *Dalton. Trans.* **2018**, *47*, 17493−17499.

(22) Cai, J.; Zheng, X.-Y.; Xie, J.; Yan, Z.-H.; Kong, X.-J.; Ren, Y.-P.; Long, L.-S.; Zheng, L.-S. Anion-Dependent Assembly of Hetero-

metallic 3d−4f Clusters Based on a Lacunary Polyoxometalate. *Inorg. Chem.* **2017**, *56*, 8439−8445.
(23) Douib, H.; Dhbaibi, K.; Lefeuvre, B.; Dorcet, V.; Guizouarn, T.; Pointillart, F. Bulky anion effect on the architecture of chiral dysprosium single-molecule magnets. *Chirality* **2023**, *35*, 155−164.
(24) Lund, H.; Bjerrum, J. Eine einfache Methode zur Darstellung wasser-freier Alkohole. *Ber. Dtsch. Chem. Ges.* **1931**, *64*, 210−213.
(25) Sheldrick, G. M. SHELXT - Integrated space-group and crystal-structure determination. *Acta Crystallogr.* **2015**, *71*, 3−8.
(26) Sheldrick, G. Crystal structure refinement with SHELXL. *Acta Crystallogr.* **2015**, *C71*, 3−8.
(27) Dolomanov, O. V.; Bourhis, L. J.; Gildea, R. J.; Howard, J. A. K.; Puschmann, H. OLEX2: a complete structure solution, refinement and analysis program. *J. Appl. Crystallogr.* **2009**, *42*, 339−341.
(28) Bruker AXS Inc. *Apex4 suite−APEX4, SAINT and SADABS*; Bruker AXS Inc.: Madison, Wisconsin, USA, 2021.
(29) van der Sluis, P.; Spek, A. L. BYPASS: an effective method for the refinement of crystal structures containing disordered solvent regions. *Acta Crystallogr.* **1990**, *A46*, 194−201.
(30) Zelazkova, J.; Jampilek, J. presented in part at the *The 15th International Electronic Conference on Synthetic Organic Chemistry*, Basel, Switzerland, 2011.
(31) Zhang, S.; Zhang, W.; Liu, X.; Wang, X.; Dong, H.; Mou, X. Synthesis method of 2,3,4-trihydroxybenzaldehyde obtained through hydroxyl protection, formylation and deprotection by using pyrogallic acid as raw material, CN117820100A, 2024.
(32) Reyes-Gutierrez, P. E.; Kapal, T.; Klepetarova, B.; Saman, D.; Pohl, R.; Zawada, Z.; Kuzmova, E.; Hajek, M.; Teply, F. Structural revisions of small molecules reported to cross-link G-quadruplex DNA in vivo reveal a repetitive assignment error in the literature. *Sci. Rep.* **2016**, *6*, 23499.
(33) Weihe, H.; Güdel, H. U. Quantitative Interpretation of the Goodenough−Kanamori Rules: A Critical Analysis. *Inorg. Chem.* **1997**, *36*, 3632−3639.
(34) Towatari, M.; Nishi, K.; Fujinami, T.; Matsumoto, N.; Sunatsuki, Y.; Kojima, M.; Mochida, N.; Ishida, T.; Re, N.; Mrozinski, J. Syntheses, Structures, and Magnetic Properties of Acetato- and Diphenolato-Bridged 3d−4f Binuclear Complexes $[M(3\text{-}MeOsaltn)(MeOH)_x(ac)Ln(hfac)_2]$ (M = Zn^{II}, Cu^{II}, Ni^{II}, Co^{II}; Ln = La^{III}, Gd^{III}, Tb^{III}, Dy^{III}; 3-MeOsaltn = N,N′-Bis(3-methoxy-2-oxybenzylidene)-1,3-propanediaminato; ac = Acetato; hfac = Hexafluoroacetylacetonato; x = 0 or 1). *Inorg. Chem.* **2013**, *52*, 6160−6178.
(35) Goura, J.; Colacio, E.; Herrera, J. M.; Suturina, E. A.; Kuprov, I.; Lan, Y.; Wernsdorfer, W.; Chandrasekhar, V. Heterometallic Zn_3Ln_3 Ensembles Containing (μ_6-CO_3) Ligand and Triangular Disposition of Ln^{3+} ions: Analysis of Single-Molecule Toroic (SMT) and Single-Molecule Magnet (SMM) Behavior. *Chem. - Eur. J.* **2017**, *23*, 16621−16636.
(36) Bartolomé, J.; Filoti, G.; Kuncser, V.; Schinteie, G.; Mereacre, V.; Anson, C.; Powell, A.; Prodius, D.; Turta, C. Magnetostructural correlations in the tetranuclear series of $\{Fe_3LnO_2\}$ butterfly core clusters: Magnetic and Mössbauer spectroscopic study. *Phys. Rev. B* **2009**, *80*, No. 014430.
(37) Sessoli, R.; Powell, A. K. Strategies towards single molecule magnets based on lanthanide ions. *Coord. Chem. Rev.* **2009**, *253*, 2328−2341.

https://doi.org/10.1021/acsomega.5c01224
ACS Omega 2025, 10, 50839−50849